Impact of Thermospheric Mass Density on the Orbit Prediction of LEO Satellites

Changyong He, Yang Yang, Brett Carter, Kefei Zhang, Andong Hu, Wang Li, Florent Deleflie, Robert Norman, Suqin Wu

AGU100 ADVANCING EARTH AND SPACE SCIENCE

Space Weather

RESEARCH ARTICLE
10.1029/2019SW002336

Impact of Thermospheric Mass Density on the Orbit Prediction of LEO Satellites

Changyong He[1,2], Yang Yang[1,2], Brett Carter[1], Kefei Zhang[1,3], Andong Hu[1,2,4], Wang Li[3], Florent Deleflie[5], Robert Norman[1,2], and Suqin Wu[3]

[1]SPACE Research Centre, School of Science, RMIT University, Melbourne, Victoria, Australia, [2]Space Environment Research Centre (SERC) Limited, Mount Stromlo Observatory, Canberra, ACT, Australia, [3]School of Environment Science and Spatial Informatics, China University of Mining and Technology, Xuzhou, China, [4]Multi-scale Group, Centrum Wiskunde and Informatica (CWI), Amsterdam, Netherlands, [5]IMCCE, Observatoire de Paris, PSL Research University, CNRS, Sorbonne Université, Univ. Lille, Paris, France

Abstract Many thermospheric mass density (TMD) variations have been recognized in observations and physical simulations; however, their impact on the low-Earth-orbit satellites has not been fully evaluated. The present study investigates the quantitative impact of periodic spatiotemporal TMD variations modulated by the empirical DTM2013 model. Also considered are two small-scale variations, that is, the equatorial mass anomaly and the midnight density maximum, which are reproduced by the Thermosphere-Ionosphere-Electrodynamics General Circulation Model. This investigation is performed through a 1-day orbit prediction (OP) simulation for a 400-km circular orbit. The results show that the impact of TMD variations during solar maximum is 1 order of magnitude larger than that during solar minimum. The dominant impact has been found in the along-track direction. Semiannual and semidiurnal variations in TMD exert the most significant impact on OP among the intra-annual and intradiurnal variations, respectively. The zero mean periodic variations in TMD may not significantly affect the predicted orbit but increase the orbital uncertainty if their periods are shorter than the time span of OP. Additionally, the equatorial mass anomaly creates a mean orbit difference of 50 m (5 m) with a standard deviation of 30 m (3 m) in 1-day OP during high (low) solar activity. The midnight density maximum exhibits a stronger impact in the order of 150 ± 30 and 15 ± 6 m during solar maximum and solar minimum, respectively. This study makes clear that careful selection of TMD variations is of great importance to balance the trade-off between efficiency and accuracy in OP problems.

Key Points:
- The impact of thermospheric mass density on the orbital dynamics of low Earth orbit has been comprehensively investigated
- The impact of periodic thermospheric mass density variations in time has also been characterized
- The EMA and MDM during different solar conditions are reproduced and analyzed using TIE-GCM

Supporting Information:
- Supporting Information S1

Correspondence to:
C. He,
changy.he@gmail.com

Citation:
He, C., Yang, Y., Carter, B., Zhang, K., Hu, A., Li, W., et al. (2020). Impact of thermospheric mass density on the orbit prediction of LEO satellites. *Space Weather*, *18*, e2019SW002336. https://doi.org/10.1029/2019SW002336

Received 23 AUG 2019
Accepted 30 OCT 2019
Accepted article online 6 NOV 2019
Corrected 7 JUL 2020

This article was corrected on 7 JUL 2020. See the end of the full text for details.

1. Introduction

Satellites in the low Earth orbit (LEO) are significantly affected by the atmospheric drag, especially for those at the altitude of 200–600 km (upper thermosphere). This perturbation force plays a critical role in mission lifetime planning, reentry prediction, collision avoidance, and attitude control. The atmospheric drag is dependent on the atmospheric mass density (ρ) and the geometry of the satellites, including the drag coefficient (C_d), mass (m), velocity ($\vec{v}$), and the projected area (A) in the direction of $\vec{v}_r$ (Vallado & McClain, 2001):

$$\vec{a}_d = -\frac{1}{2}\rho\, C_d\, \frac{A}{m}\, \|\vec{v}_r\|\, \vec{v}_r, \tag{1}$$

$$\vec{v}_r = \vec{v} - \vec{v}_w, \tag{2}$$

where $\vec{v}$ is the velocity of the satellite and $\vec{v}_r$ is the relative velocity of the satellite with respect to the wind $\vec{v}_w$. In the orbit prediction (OP) simulation performed in this study, these equations are evaluated in the Earth-centered inertial frame.

Empirical thermospheric mass density (TMD) models can be used for atmospheric drag calculations, for example, NRLMSISE-00 (Naval Research Laboratory Mass Spectrometer Incoherent Scatter Radar Series) (Picone et al., 2002), JB2008 (Jacchia-Bowman) (Bowman et al., 2008), and DTM2013 (Drag Temperature Model) (Bruinsma, 2015). Accurate TMD prediction is critical in the tracking and collision avoidance of LEO satellites. The error of empirical TMD models is one of the largest sources of uncertainty in OP for LEO

objects. This error was found to be 15–30% on average, under most conditions (Doornbos, 2012; Shi et al., 2015), while it can reach up to 100% during extreme space weather conditions (Doornbos et al., 2008), for example, geomagnetic storms and solar flares. A comprehensive review and comparison of commonly used empirical TMD models can be found in Emmert (2015b) and He et al. (2018).

Due to the increasing number of TMD measurements from LEO satellites, many variations in TMD have been recognized and investigated. For example, Qian and Solomon (2012) examined the temporal variations in TMD with temporal scales ranging from decades to hours. These variations include the solar cycle (11-year); annual and semiannual; solar rotation (27-day); diurnal, semidiurnal, and terdiurnal variations; and abrupt changes associated with solar flares and geomagnetic storms. Xu et al. (2013) found strong longitudinal variations in the daily-mean TMD with a seasonal pattern and an annual oscillation.

Historical TMD data sets collected by LEO satellites, such as the Challenging Minisatellite Payload (CHAMP) and Gravity Recovery and Climate Experiment (GRACE) satellites, have revealed an equatorial pattern called the equatorial mass density anomaly (EMA), that is, TMD peaks at magnetic low-to-middle latitudes (±25°) and a trough near the geomagnetic equator at 10–20 LT (Liu et al., 2017). The difference of TMD between trough and crest in EMA was reported by Liu et al. (2017) to be approximately 1–6%. EMA variability was found to be associated with ionospheric forcing, and hence, it is aligned to the well-known equatorial temperature anomaly and equatorial ionization anomaly in the ionosphere (Liu et al., 2017). The physical mechanics of the trough and crests in the EMA are different. The ion drag parallel to the geomagnetic field, that is, the field-aligned ion drag, was found to be the main contributor to the trough of EMA (Lei et al., 2012). However, no full explanation has been entirely confirmed for the EMA crests. Possible causes include the plasma-neutral heating (Lei et al., 2012), the diurnal tide, and the upward propagating terdiurnal tide (Lei et al., 2011; Miyoshi et al., 2011).

The midnight mass density maximum (MDM) is another interesting phenomenon in the thermosphere with a nighttime enhancement in TMD near the geographic equator after midnight. It is also related to the midnight temperature maximum. The MDM has been observed from both the ground and satellites since the 1970s (Ruan et al., 2014). Recent studies show that both the upward semidiurnal and terdiurnal tides from the lower atmosphere contribute to the MDM (Ruan et al., 2015).

Although many TMD variations have been intensively studied in recent years, their quantitative impact on the orbital dynamics has not been fully investigated. For example, Lechtenberg et al. (2013) examined the traveling atmospheric disturbances, geomagnetic cusp, and MDM in the TMD derived from precise orbits and accelerometer measurements of GRACE and CHAMP. However, the impact of these three TMD variations on the orbit propagation results was not separated. Moreover, many complex temporal and spatial TMD variations (e.g., EMA and MDM) may have discernible impacts on orbital dynamics in LEO and are not yet emulated in the empirical models. Leonard et al. (2012) was the first to assess the error in the 1-day OP incurred by ignoring the migrating tides (longitude-dependent tides) in LEO. Their results showed a three-dimensional (3-D) orbit difference of approximately 15 km and 200 m at the altitudes of 200 and 400 km, respectively. This result was limited to the moderate solar condition $F_{10.7} = 110$ solar flux unit (sfu) (Leonard et al., 2012).

Additionally, there is a trade-off between efficiency and accuracy in space situation awareness. Petit and Lemaitre (2016) showed that DTM2013 obtained a slightly better result but with almost 50 times more computational resources than that of JB2008 in the long-term OP of Starlette and Stella satellites (~800 km). Due to the heavy computations behind the accurate prediction of the TMD and atmospheric drag, many studies in the orbital uncertainty propagation only consider a simplified TMD model in which the TMD is only dependent on the altitude of the satellite (e.g., Giza et al., 2009).

The present study aims to identify the quantitative impact of TMD variations on the orbital dynamics of LEO satellites. Suggestive directions are formulated for balancing the efficiency and accuracy of OP. Moreover, different from the studies of space physics and the upper atmosphere, which are interested in the mechanics of the TMD variations, this study focuses on the TMD variations, the uncertainty from the imperfect empirical TMD models, and their accumulative impact on the LEO dynamics. The outline of this study is given as follows. First, section 2 introduces the empirical and physical models used to simulate the TMD variations in this study. Section 3 elaborates the temporal (intra-annual and intradiurnal), spatial (latitudinal and longitudinal), and physic-based (EMA and MDM) variations of the TMD considered in this study. Section 4

investigates the impact of TMD variations through 1-day OP simulations at the altitude of 400 km. The final section summarizes the impact of these TMD variations and discusses the selection of TMD variations in the operational problem with the required accuracy.

2. TMD Simulations

Two different TMD models, that is, DTM2013 and the Thermosphere-Ionosphere-Electrodynamics General Circulation Model (TIE-GCM), are used to capture the TMD variations considered in this study. In these simulations, the values of the $F_{10.7}$ and K_p indices used for both DTM2013 and TIE-GCM are fixed to 200sfu (70sfu) and 1, representing the solar maximum (minimum) and the quiet geomagnetic condition, respectively. Note that the constant $K_p = 1$ used here aims to separately determine the solar impact by minimizing the geomagnetic impact.

2.1. DTM2013

DTM2013 is one of the most commonly used empirical TMD models representing the statistical average status of the atmosphere in the altitude range of 120–1,500 km (Bruinsma, 2015). Based on the spherical harmonic expansion technique, the DTM-2013 model outputs the atmospheric neutral temperature and mass density along with the concentrations of atmospheric components including N_2, O_2, He, O, and H. The inputs of DTM2013 include the day of the year (DOY), local time, geodetic coordinates, and the $F_{10.7}$ and K_p indices. Note that these space weather indices are optional for DTM2013. If those indices are not specified by the users, DTM2013 will use default indices such as F_{30} and K_m which may provide a better performance (de Wit et al., 2014; de Wit & Bruinsma, 2017).

2.2. TIE-GCM

The TIE-GCM is a 3-D, time-dependent and self-consistent physical model developed by the High Altitude Observatory in National Center for Atmospheric Research (Richmond et al., 1992; Sutton et al., 2015). It can simulate the nonlinear coupling between the thermosphere and ionosphere. In the vertical direction, TIE-GCM is modeled based on the pressure levels roughly extending from ~90 to 500–700 km, depending on the level of solar activity.

From the TIE-GCM simulations under high solar activity ($F_{10.7} = 180$ sfu), Lei et al. (2012) confirmed that the field-aligned ion drag has a critical impact on the formation of EMA peaks but it is only slightly associated with the EMA crests. The momentum equation used in the TIE-GCM v2.0 can be written as (Foster, 2016; Hsu et al., 2014)

$$\frac{\partial \vec{w}}{\partial t} = \left(\vec{g} - \frac{1}{\rho}\nabla P\right) - 2\,\vec{\omega}_{\oplus} \times \vec{w} - \vec{\omega}_{\oplus} \times \left(\vec{\omega}_{\oplus} \times \vec{r}\right) - \vec{w} \cdot \nabla \vec{w} - \frac{1}{\rho}\nabla\left(\mu_c \nabla \vec{w}\right) - \nu_{ni}(\vec{w} - \vec{w}_i), \tag{3}$$

where $\vec{w}$ is the neutral wind velocity at the location $\vec{r}$, both in the geographic frame; $\vec{g}$ is the gravitational acceleration; $\vec{\omega}_{\oplus}$ is the angular velocity of the Earth; μ_c is the viscosity coefficient; ν_{ni} is the neutral-ion collision frequency; $\vec{w}_i$ is the ion velocity; and the other variables are the same as previously defined. Note that the neutral wind velocity in TIE-GCM is defined in the Earth-centered Earth-fixed frame, whereas the previous one in equation (2) is defined in the Earth-centered inertial frame. The terms on the right side are the accelerations due to the nonhydrostatic effect, Coriolis force, centrifugal force, horizontal advection, viscosity, and ion drag. It is worth noting that TIE-GCM is based on the hydrostatic assumption, which simplifies the momentum equation by changing the vertical component to the geopotential of pressure levels.

The ion drag can be further expressed as the sum of two components perpendicular ($\perp$) and parallel ($\|$) to the geomagnetic field (Lei et al., 2012; Zhu et al., 2005):

$$-\nu_{ni}(\vec{w} - \vec{w}_i) = -\nu_{ni}\,(\vec{w}_{\perp} - \vec{w}_{i\perp}) - \nu_{ni}\,(\vec{w}_{\|} - \vec{w}_{i\|}) = \frac{\vec{J} \times \vec{B}}{\rho} - \nu_{ni}\,(\vec{w}_{\|} - \vec{w}_{i\|}), \tag{4}$$

where $\vec{J}$ is the electric current density; subscript "$\|$" is the component parallel to $\vec{B}$; and the first and the last terms on the right side of this equation are the Lorentz force per unit mass and the field-aligned ion drag, respectively. Lei et al. (2012) further showed that the plasma-neutral heating (collision heating between

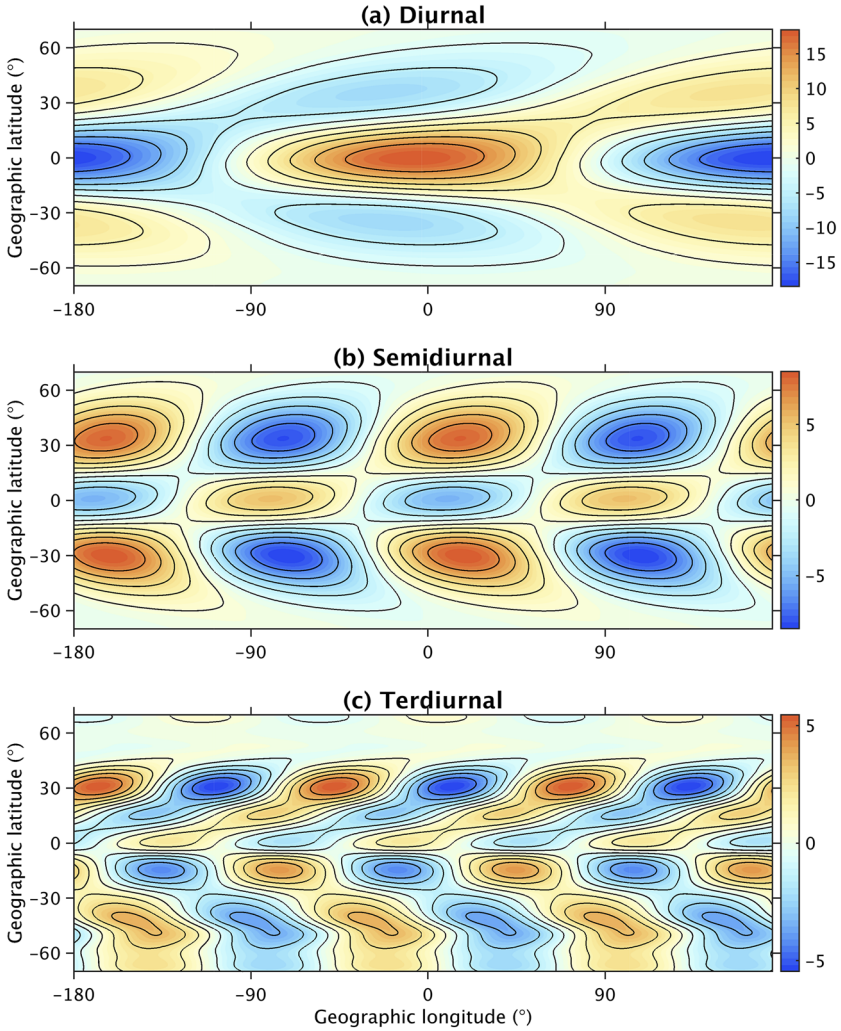

Figure 1. An example of atmospheric tides in neutral temperature (unit: K). The migrating (a) diurnal and (b) semidiurnal tides are predicted by GSWM and the migrating (c) terdiurnal tide by eCMAM at the lower boundary of TIE-GCM (~99 km).

neutrals and charged particles) can explain the equatorial temperature anomaly crests. Note that the latest version of TIE-GCM (v2.0) does not consider the mechanism of field-aligned ion drag proposed by Lei et al. (2012).

In this study, four TIE-GCM simulations are run for the DOYs of 80, 172, 264, and 355, representing two equinoxes (March and September) and two solstices (June and December). To reproduce the EMA and MDM, the TIE-GCM is simulated with a time step of 30 s, a horizontal resolution of 5°, and a constant eddy diffusion at the lower boundary of ~99 km. The lower boundary of neutral temperature and wind velocity are set by the Global-Scale Wave Model Hagan and Forbes (2002) and extended Canadian Middle Atmosphere Model McLandress et al. (2006). An example of the diurnal, semidiurnal, and terdiurnal tides of neutral temperature at 12 UTC during the March equinox for the lower boundary of TIE-GCM (~99 km) is shown in Figure 1.

To obtain a steady state of TIE-GCM, the simulation starts at 5 days before the date of OP simulations. As shown in Table 1, $F_{10.7}$ = 70sfu ($F_{10.7}$ = 200sfu) represents the solar minimum (maximum) during geomagnetic quiet time (K_p = 1). The upward propagating terdiurnal tide from the troposphere, as one of possible EMA drivers found by Miyoshi et al. (2011), is not considered in the simulations of Runs 1 and 2. Referring to Figure 2a, the latitudinal TMD variation at five different longitudes during March equinox derived from Run 2 in Table 1 shows a clear trough pattern near the geomagnetic dip equator indicated

Table 1
Settings of the TIE-GCM Simulations for Solar Maximum ($F_{10.7}$ = 200) and Solar Minimum ($F_{10.7}$ = 70) During Geomagnetic Quiet Time (K_p = 1)

Run	$F_{10.7}$	Field-aligned ion drag	Diurnal and semidiurnal tides	Terdiurnal tide
1	70/200	—	✓	—
2	70/200	✓	✓	—
3	70/200	—	—	—
4	70/200	—	✓	✓

by the black dash line. EMA patterns during other seasons in Figures 2b–2d are not examined in Lei et al. (2012) and Hsu et al. (2014) but are still discernible.

3. Variations in TMD

The thermosphere is an extremely complicated nonlinear system that couples with the ionosphere and the magnetosphere. The primary sources of input energy into the thermosphere are solar irradiance and solar

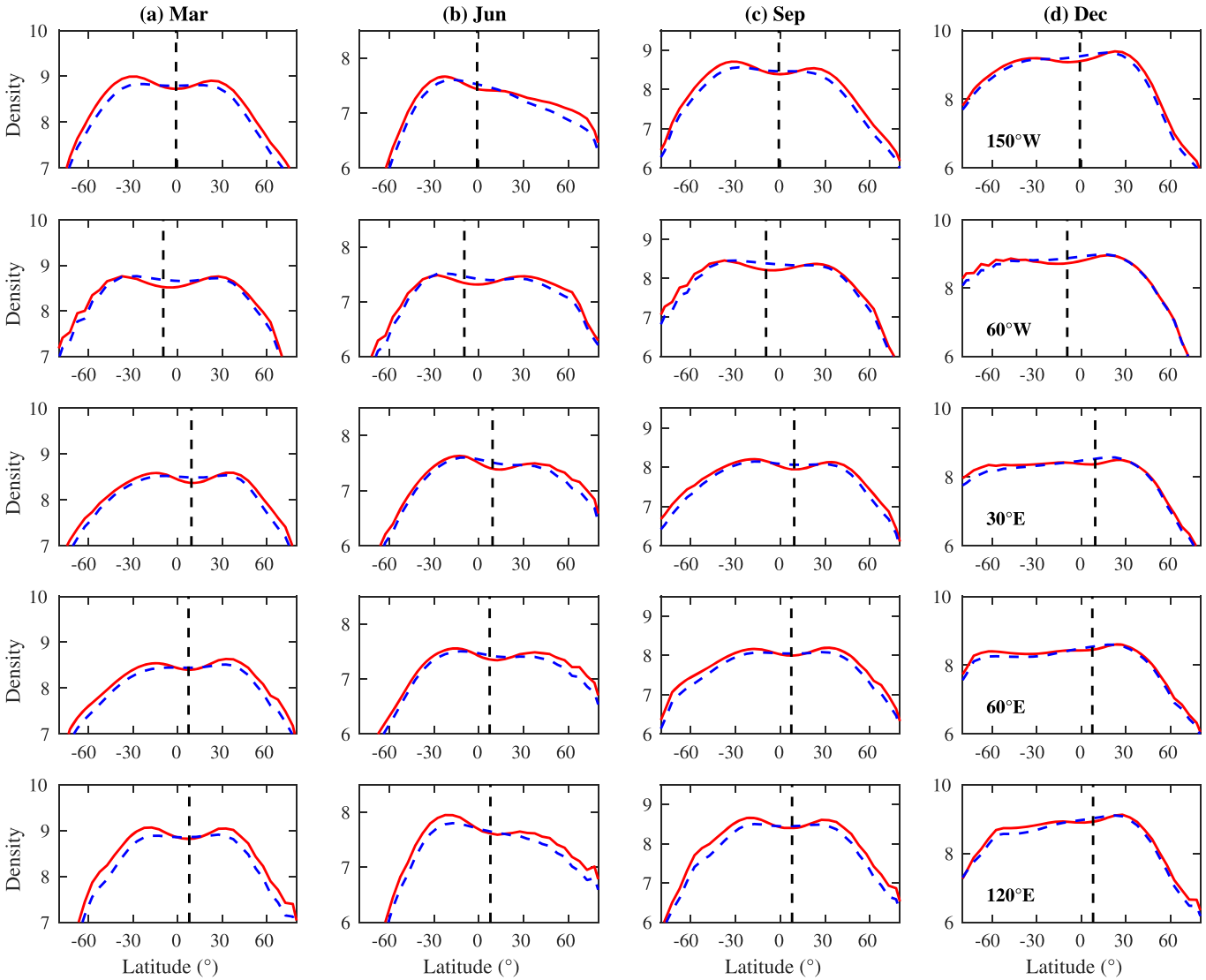

Figure 2. Latitudinal distribution of TMD (unit: 10^{-12} kg/m^3) in EMA simulated by Runs 1 (blue) and 2 (red) at (a) March equinox, (b) June solstice, (c) September equinox, and (d) December solstice during high solar activity ($F_{10.7}$ = 200sfu). Four rows from top to bottom represent the TMD at the longitudes of 150°W, 30°E, 60°E, and 120E. Black dash line indicates the geomagnetic dip equator determined by IGRF12.

Table 2
The Percentage Variation of TMD Relative to the Long-Term Mean Value at the Altitude of 400 km

Variation	Amplitude (%)	Features (period/latitude)
Long-term decrease	1–5	per decade
Solar cycle	~100	11 years
Solar rotation	<100	27 days, decrease for lower solar activity
Annual	5–15	1 year
Semiannual	~20	0.5 year
Diurnal	10–40	24 hr
Semidiurnal	~10	12 hr
Terdiurnal	0–3	8 hr
Geomagnetic Storms	100–200	<1 hr
Latitudinal	10–20	—
Longitudinal	<5	—
MDM	20–30	23–01 LT, 20° N to 20° S
EMA	1–6	10–20 LT, 30° N to 30° S

Note. The data for the intra-annual and intradiurnal variations are derived from DTM2013 and the others from Emmert (2015b) and Qian and Solomon (2012).

wind in the form of protons, helium, and other charged/neutral particles (Hargreaves, 1992). Thus, TMD, to a large extent, is determined by solar activity. On the other hand, the geomagnetic activity, caused by the interaction between the geomagnetic field and the solar wind plasma (Qian & Solomon, 2012), also generates additional short-term variations in TMD.

Table 2 lists the percentage variations of TMD relative to the long-term mean value from DTM2013 and previous literature (e.g., Emmert, 2015b; Liu et al., 2017; Qian & Solomon, 2012). Compared to the global warming effect in troposphere, the middle and upper atmosphere experience a cooling effect due to the loss of collision energy in the infrared radiance. A long-term trend of TMD as shown in Table 2 has been confirmed by satellite drag measurements and model simulations (Emmert, 2015a) and was found associated with the increasing concentration of CO_2 (Emmert, 2015a; Qian & Solomon, 2012). This long-term decrease of TMD is not considered in this study due to its limited magnitude. In this study, the EMA and MDM are reproduced by TIE-GCM. The other TMD variations are simulated by DTM2013. To examine the impact of TMD variations independently, separate derivation of each TMD variation will be presented in this section.

3.1. Temporal Variations

The TMD includes temporal variations due to, for example, the 11-year solar cycle, the 27-day solar rotation, the Earth's revolution, and the Earth's rotation. This study only considers the classic annual, semiannual, and diurnal oscillations, which are simulated by DTM2013. The impact of other longer-period TMD variations due to solar activity is evaluated by comparing the OP results during solar maximum and solar minimum conditions in this study.

3.1.1. Intra-annual

Intra-annual variations in TMD and atmospheric compositions exhibit two maxima near two equinoxes (March and September), one major minimum in June and one minor minimum in January (Emmert, 2015b). Figure S1 from the supporting information shows the geographic latitude versus DOY of percentage TMD variation predicted by DTM2013 at the altitude of 200 and 400 km. In this study, the solar maximum and solar minimum have been set to 200 and 70sfu, respectively. The DOY of two annual maxima in the model-derived TMD at 400 km varies slightly with the seasons, but it barely changes at 200 km. The amplitudes of intra-annual variations were found to have a positive correlation with geomagnetic and solar activities (Emmert, 2015b; Guo et al., 2008). In this study, annual and semiannual variations at a given position can be expressed by

$$\rho_a(DOY) = \bar{\rho}_a + A_1 \sin\left(\frac{2\pi\ DOY}{365.25}\right) + B_1 \cos\left(\frac{2\pi\ DOY}{365.25}\right) + A_2 \sin\left(\frac{4\pi\ DOY}{365.25}\right) + B_2 \cos\left(\frac{4\pi\ DOY}{365.25}\right), \quad (5)$$

where $\bar{\rho}_a$ is the annual mean TMD; A_i and B_i ($i = 1, 2$) are the coefficients for the annual and semiannual variations (equivalent to the amplitudes and phases). Smaller-scale variations are neglected in this equation. Once the coefficients are estimated using the least squares, one specific variation can be removed by setting the corresponding coefficients to zero.

3.1.2. Intradiurnal

The most prominent intradiurnal variations of TMD are diurnal, semidiurnal, and terdiurnal variations with the periods of 24, 12, and 8 hr, respectively. The diurnal variation in the upper thermosphere mainly results from the daily variability of solar irradiance (Qian & Solomon, 2012). Forbes et al. (2009) also presented the alignment of the diurnal variation in the lower thermosphere with the upward propagating tides from troposphere.

The LT versus geographic latitude distribution of percentage variation in DTM2013-derived TMD is illustrated in Figure S2. During both solar maximum and solar minimum, the daily peak in TMD appears near 14 LT. The TMD in the daytime is larger than that in the nighttime except for the TMD at 200 km. This result may indicate the imperfect modeling of DTM2013 at lower altitudes during high solar activity. Therefore, the altitude of 200 km is not considered in the following OP simulation. The EMA feature is captured during solar maximum between 12 and 16 LT, which will be further discussed in section 3.3.

Intradiurnal variations have been considered in many popular empirical TMD models, for example, the DTM-class models (Berger et al., 1998; Bruinsma et al., 2003; Bruinsma, 2015). Analogous to equation (5), first three intradiurnal TMD variations at given location can be expressed as a function of LT (or UT):

$$\begin{aligned}\rho_d(LT) = \bar{\rho}_d &+ C_1 \sin\left(\frac{2\pi\ LT}{24}\right) + D_1 \cos\left(\frac{2\pi\ LT}{24}\right)\\ &+ C_2 \sin\left(\frac{2\pi\ LT}{12}\right) + D_2 \cos\left(\frac{2\pi\ LT}{12}\right)\\ &+ C_3 \sin\left(\frac{2\pi\ LT}{8}\right) + D_3 \cos\left(\frac{2\pi\ LT}{8}\right),\end{aligned}$$

where C_i and D_i ($i = 1, 2, 3$) are the coefficients representing the amplitudes and phases of variations. Again, smaller-scale variations are neglected, and one type of variation can be removed by setting the corresponding coefficients to zero.

3.2. Large-Scale Spatial Variations

The TMD decreases exponentially with the increasing altitude (diffusive equilibrium state), even though the hydrostatic equilibrium may not be satisfied due to the global circulation of the thermosphere such as the nonmigrating tides (Qian & Solomon, 2012). Solar irradiance is the dominant energy input to the Earth's atmosphere; the TMD peak is, therefore, located close to the subsolar point (at the local noon). In this study, this LT effect has been removed from the longitudinal variation of TMD. Figure S3 illustrates the global horizontal TMD of geographic latitude versus geographic longitude predicted by DTM2013 at 12 UTC. Note that the longitudinal variation illustrated has removed the contribution of LT, which will be explained later. One may notice that the latitudinal variation in TMD is larger than the longitudinal variation.

3.2.1. Latitudinal

Latitudinal variation is generated by the global atmospheric circulation (neutral wind) that is excited mainly by the solar irradiance, geomagnetic activity, and Earth's rotation. This circulation transports energy and atmospheric components to different latitudes. Moreover, other factors can also affect the latitudinal distribution of TMD such as the Sun-Earth distance and the coupling effect between thermosphere and ionosphere. For the same LT and altitude, TMD can be decomposed into

$$\rho(\lambda, \varphi) = \bar{\rho}_\varphi(\lambda) + \Delta\ \rho_\varphi, \tag{6}$$

where λ and φ are the geographic longitudes and latitudes, respectively; $\bar{\rho}_\varphi$ is the latitudinal mean TMD (weighted by the cosine of the latitude)

$$\bar{\rho}_\varphi(\lambda) = \frac{1}{2}\int_{-\frac{\pi}{2}}^{\frac{\pi}{2}} \rho(\lambda, \varphi)\ \cos\varphi\ \mathrm{d}\varphi, \tag{7}$$

and $\Delta\ \rho_\varphi$ is the latitudinal variation in TMD. Again, other TMD variations and errors are neglected here. The latitudinal variation can be removed by averaging the DTM2013-derived TMD over 90° N to 90° S under the same longitude, local time, altitude, and space weather conditions.

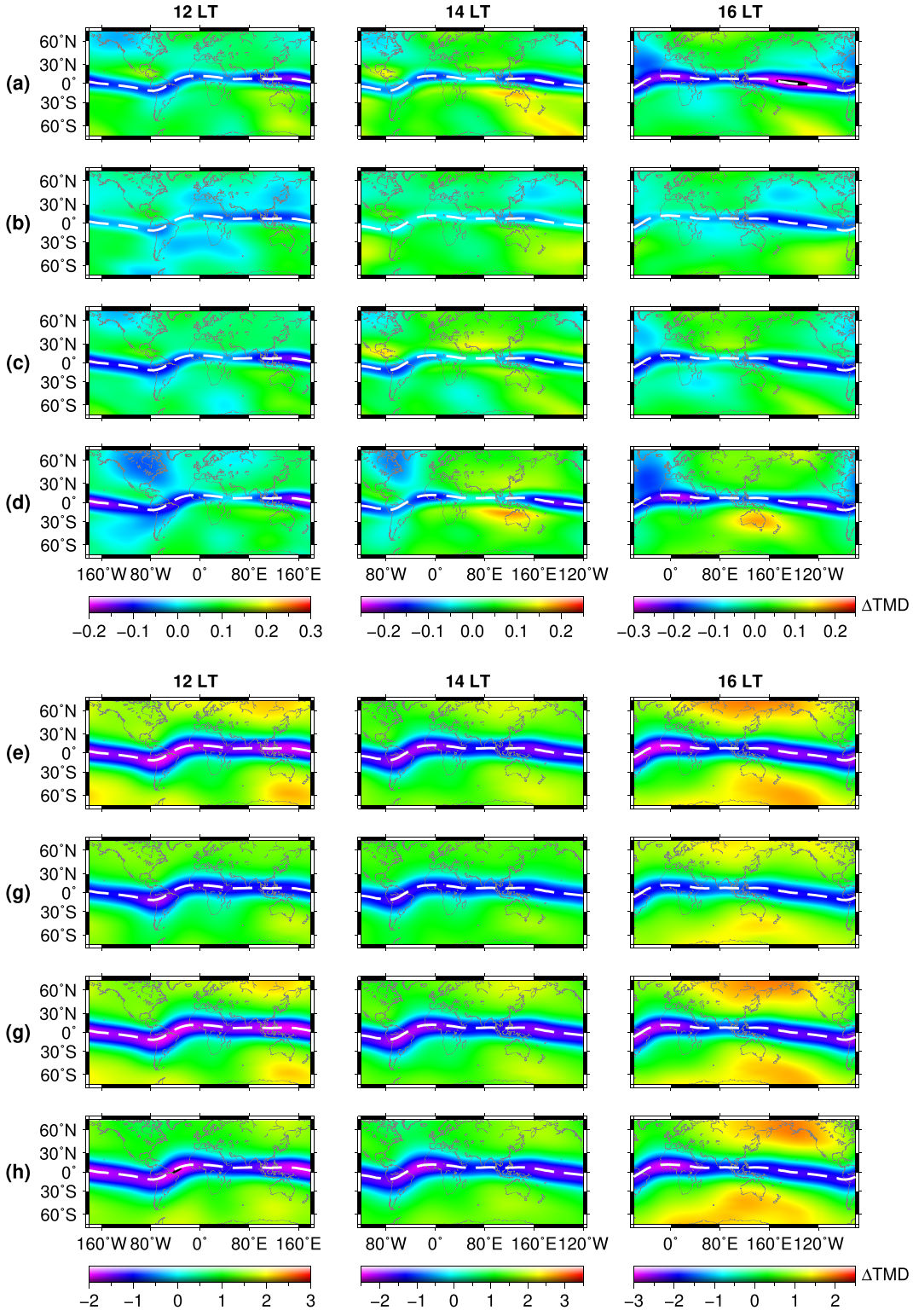

Figure 3. Latitudinal and LT distribution of TMD difference (unit: 10^{-13} kg/m^3) at 400 km (Runs 1 − Run 2) during solar minimum (70sfu) at (a) March equinox, (b) June solstice, (c) September equinox, and (d) December solstice. The corresponding result for four seasons during solar maximum are presented in (e)–(h). White dash lines indicate the geomagnetic dip equator.

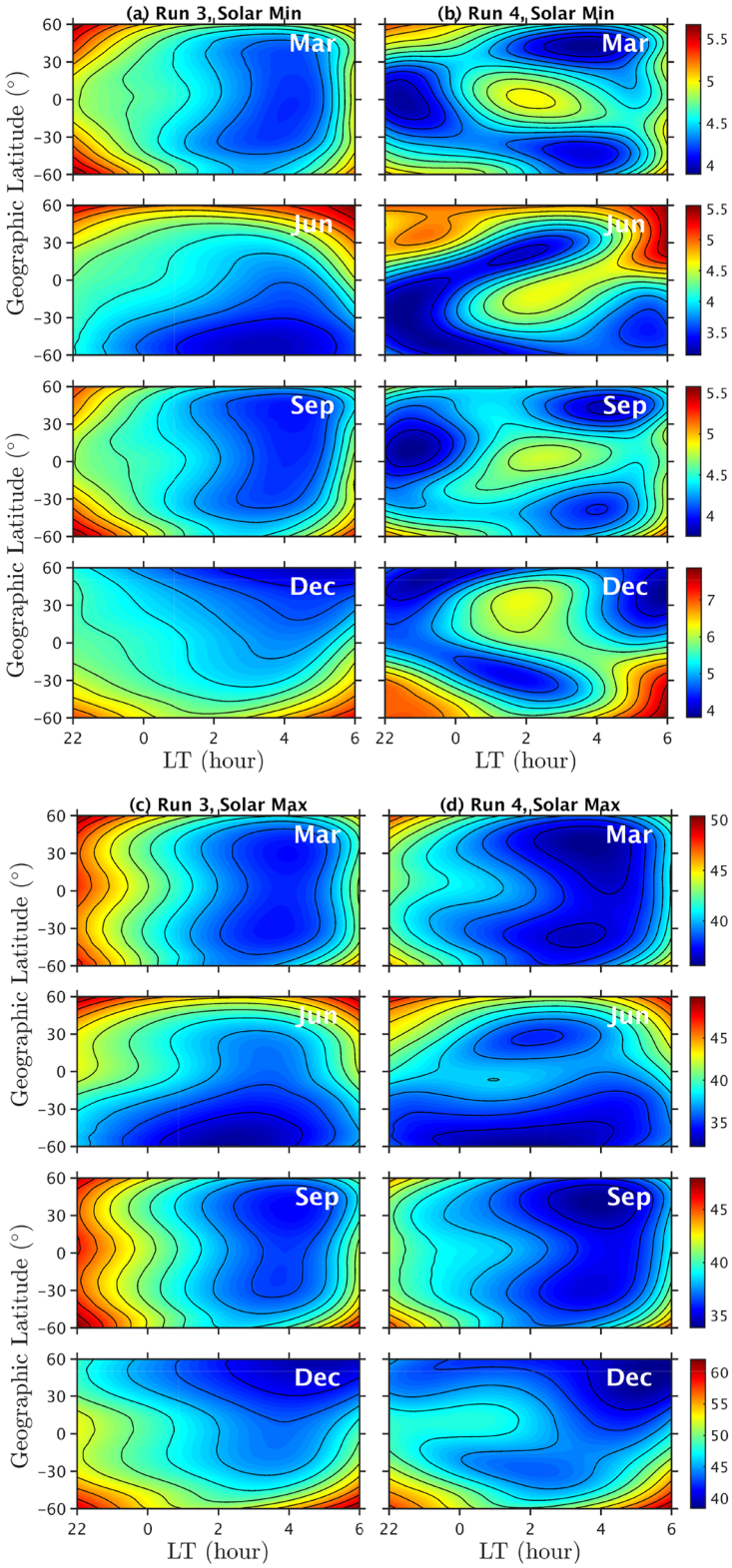

Figure 4. Latitudinal and LT distribution of MDM (unit: 10^{-13} kg/m^3) at 400 km simulated by Run 3 during solar minimum (a) and solar maximum (c) and by Run 4 during solar minimum (b) and solar maximum (d). The solar maximum and minimum are simulated by setting $F_{10.7}$ to 200 and 70sfu, respectively. Four rows from the top to bottom in each panel indicate March, June, September, and December.

Table 3
Models Used for the Evaluation of TMD Variations in OP

Configuration	Description
Geopotential	ITG-Grace2010s (Static gravity model, degree 100) (Mayer-Guerr et al., 2010)
N-body	JPL DE430 ephemeris
Solid Earth (pole) tide	IERS 2010 conventions (Petit & Luzum, 2010)
Ocean (pole) tide	FES2004 (degree 50) (Petit & Luzum, 2010)
Precession and Nutation	IAU2000 (Petit & Luzum, 2010)
Earth orientation parameters	IERS EOP14 C04 data
Solar radiation pressure	Cannon-ball model (A=0.5 m^2, m = 500 kg and radiation coefficient C_r = 1.3)
Atmospheric drag	TIE-GCM and DTM2013 (A = 0.5m^2, m = 500 kg and C_d = 2.3)
Horizontal wind	HWM14 (Drob et al., 2015)
Propagator	Variable-step, variable-order Adams-Bashforth-Moulton algorithm for deterministic OP (absolute tolerance 10^{-10} and relative tolerance 10^{-13}, adaptive time step);
	Runge-Kutta algorithm for stochastic OP (fixed time step of 0.1 s) (Kasdin, 1995).

3.2.2. Longitudinal

Longitudinal variation of TMD is a periodic change through 360° in longitude. This variation has been found highly correlated to the tides in the thermosphere and the Joule particle heating in the auroral region (Xu et al., 2013). The tides here refer to the nonmigrating tides that are planetary-scale tidal waves with a harmonic period of 1 day and does not propagate with the apparent motion of the Sun (Emmert, 2015b). An example of longitudinal variation is given by Figure S3, from which Wave Number 3 and Wave Number 4 patterns are observable (three or four troughs of TMD in the zonal direction). These patterns have been widely confirmed by numerical simulations and observations at the low latitude and equatorial regions (Xiong et al., 2015).

In the same way, the longitudinal TMD at the given LT (or UT) and altitude can be expressed as follows:

$$\rho\ (\lambda, \varphi) = \bar{\rho}_{\lambda}(\varphi) + \Delta\ \rho_{\lambda}, \tag{8}$$

$$\bar{\rho}_{\lambda}(\varphi) = \frac{1}{2\pi} \int_{-\pi}^{\pi} \rho(\lambda, \varphi)\ \mathrm{d}\lambda, \tag{9}$$

where $\bar{\rho}_{\lambda}$ is the longitudinal mean TMD and $\Delta\rho_{\lambda}$ is the longitudinal variation in TMD. Likewise, the longitudinal variation is removed by averaging over 180° W to 180° E under the same latitude, local time, altitude, and space weather conditions.

3.3. EMA and MDM

As two examples of low-to-middle latitudinal variability of TMD, the EMA and MDM include both temporal and spatial variations. The previous large-scale variations are investigated using DTM2013, whereas these two "smaller-scale" variations are reproduced using TIE-GCM. The spatiotemporal feature of EMA and MDM is usually due to the complicated physical dynamics in the atmosphere. Although the dynamics of these spatiotemporal variations may not be of great interest to OP applications, they show a nonnegligible impact on orbital dynamics (see section 4.3).

As shown in Table 1, the distribution of TMD difference between Runs 1 and 2 (Run 1 − Run 2) are illustrated in Figures 3a–3d and 3e–3h for four seasons during solar minimum and solar maximum, respectively.

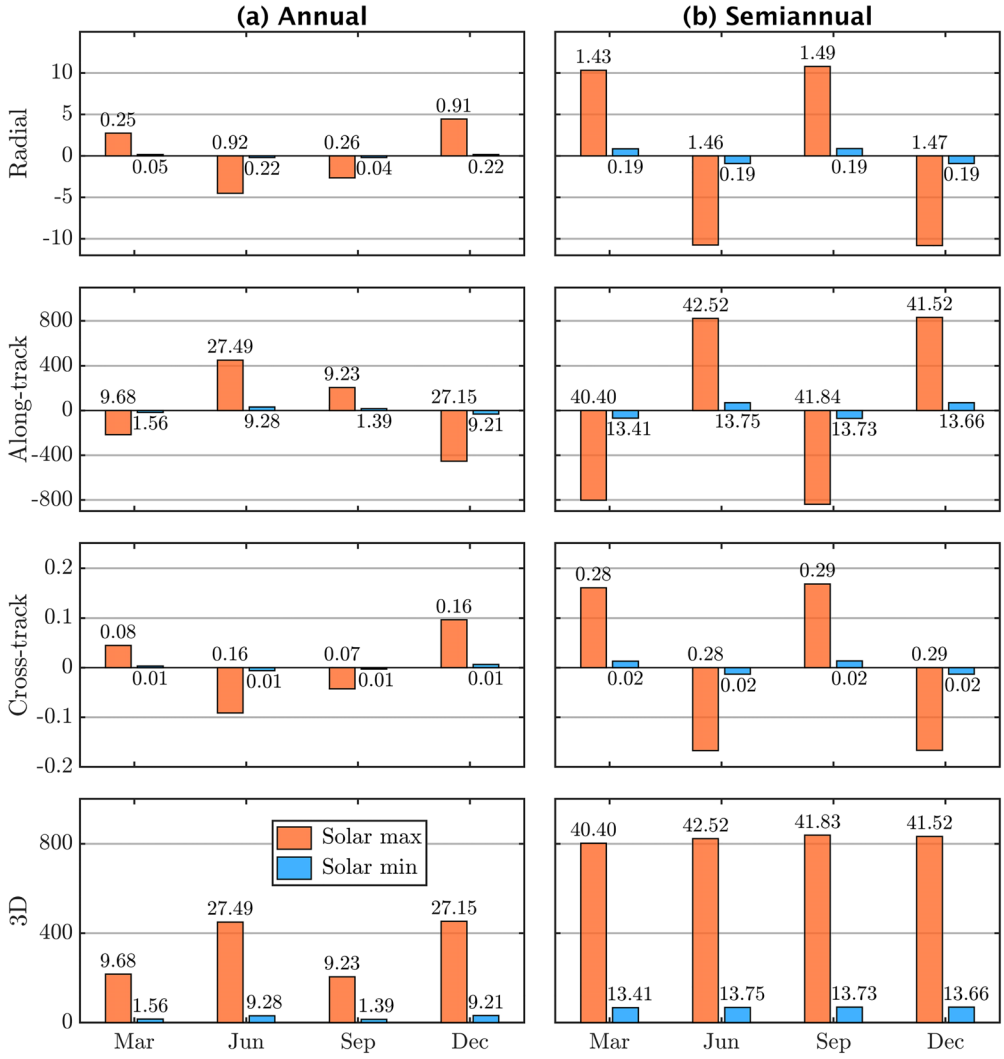

Figure 5. Impact of (a) annual and (b) semiannual variations in TMD on 1-day OP at the altitude of 400 km during solar maximum and solar minimum (unit: m). The bars show the mean value of orbit difference between the control and reference orbits in radial, along-track, and cross-track directions along with the three-dimensional (3-D) value. The values over/under the bar are the STD of orbit difference.

A clear strip-shaped area of low TMD distributed along the geomagnetic dip equator can be observed during solar maximum (Figures 3e and 3f) due to the trough in EMA. The EMA becomes much weaker during solar minimum, while it is still discernible especially during the equinoxes as shown in Figures 3a and 3c.

As introduced in section 2, the MDM is replicated by adding diurnal, semidiurnal, and terdiurnal tides to TIE-GCM. Figure 4 shows the longitudinally averaged TMD near the midnight during both solar minimum and solar minimum. The MDM phenomenon during solar minimum (Figure 4b) has been analyzed and confirmed by Ruan et al. (2014, 2015). Evidently, an equatorial nighttime enhancement in TMD can be found during solar maximum as shown in Figure 4d.

4. Numerical Analysis Based on OP

The impact of different TMD variations is evaluated in 1-day OP simulations. The configurations of OP are listed in Table 3. A drag coefficient of $C_d = 2.3$ for a spherical satellite is assumed. The assumed value of C_d will insignificantly affect the consistency of the final OP-based results although drag coefficients for other satellites may increase or decrease the orbit difference (Leonard et al., 2012). Also, a mass of 500 kg along with a projected area of 0.5 m^2 is used based on the geometry of the GRACE satellite. The Earth-reflected radiation and the Earth-emitted radiation are neglected in the OP simulation.

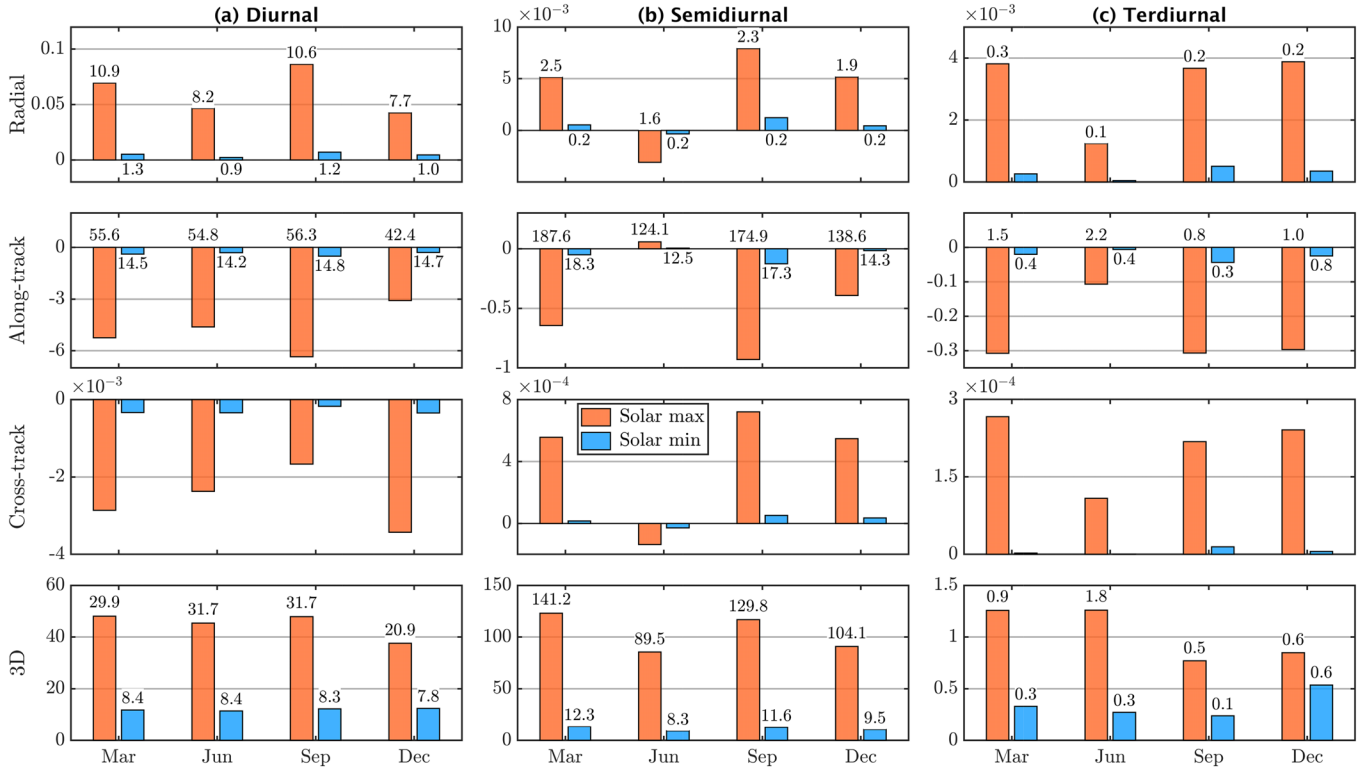

Figure 6. Impact of (a) diurnal, (b) semidiurnal, and (c) terdiurnal variations in TMD on 1-day OP at the altitude of 400 km during solar maximum and solar minimum (unit: m). The bars show the mean value of orbit difference between the control and reference orbits in radial, along-track, and cross-track directions along with the three-dimensional (3-D) value. The values over/under the bar are the STD of orbit difference larger than 1 cm.

A set of 30 orbits with different ascending nodes is examined during each season (March, June, September, and December). The ascending nodes of these 30 orbits are equally spaced at the equator, which indicates the different LT/LST for the initial epoch of OP simulations. Three inclination angles (0°, 45°, and 90°) of the orbits are examined for analyzing the impact of the latitudinal distribution of TMD.

The impact of TMD variations is evaluated using the orbit difference between the predicted orbits with and without the specific TMD variation. The results are investigated based on the mean and standard deviation (STD) of orbit difference over 30 × 3 (ascending node × inclination) simulations. The orbit difference is the difference between the "control" and the "reference" orbits predicted without and with the specific TMD variation, respectively.

4.1. Temporal Impact

Figure 5 illustrates the results of the 1-day OP disturbed by intra-annual variations during different solar activity periods. The orbit difference is analyzed in radial, along-track, and cross-track directions. In general, variations in TMD have the largest impact on the OP in the along-track direction and the smallest impact in the cross-track direction, since the drag acceleration is oriented in the opposite direction to the satellite's motion. The mean 3-D orbit difference due to annual variation during solar maximum (200–400 m) is approximately 1 order of magnitude larger than that during solar minimum (1–10 m) (see Figure 5a). The mean value of the orbit difference is larger than its STD, implying that the intra-annual variations have a more significant impact on the mean value of the predicted orbit than that on the uncertainty.

The positive mean values of orbit difference in the along-track direction indicate a smaller atmospheric drag experienced by the satellite and, hence, a smaller TMD in the OP. Annual variation decelerates the orbital decay in June and September but accelerates the decay in March and December as shown in Figure 5a. As observed in Figure 5b, the semiannual variation decelerates the orbital decay near the solstices and accelerates near the equinoxes, which agrees with the previous studies that two maxima and two minima exhibit near the equinoxes and the solstices, respectively (Emmert, 2015b).

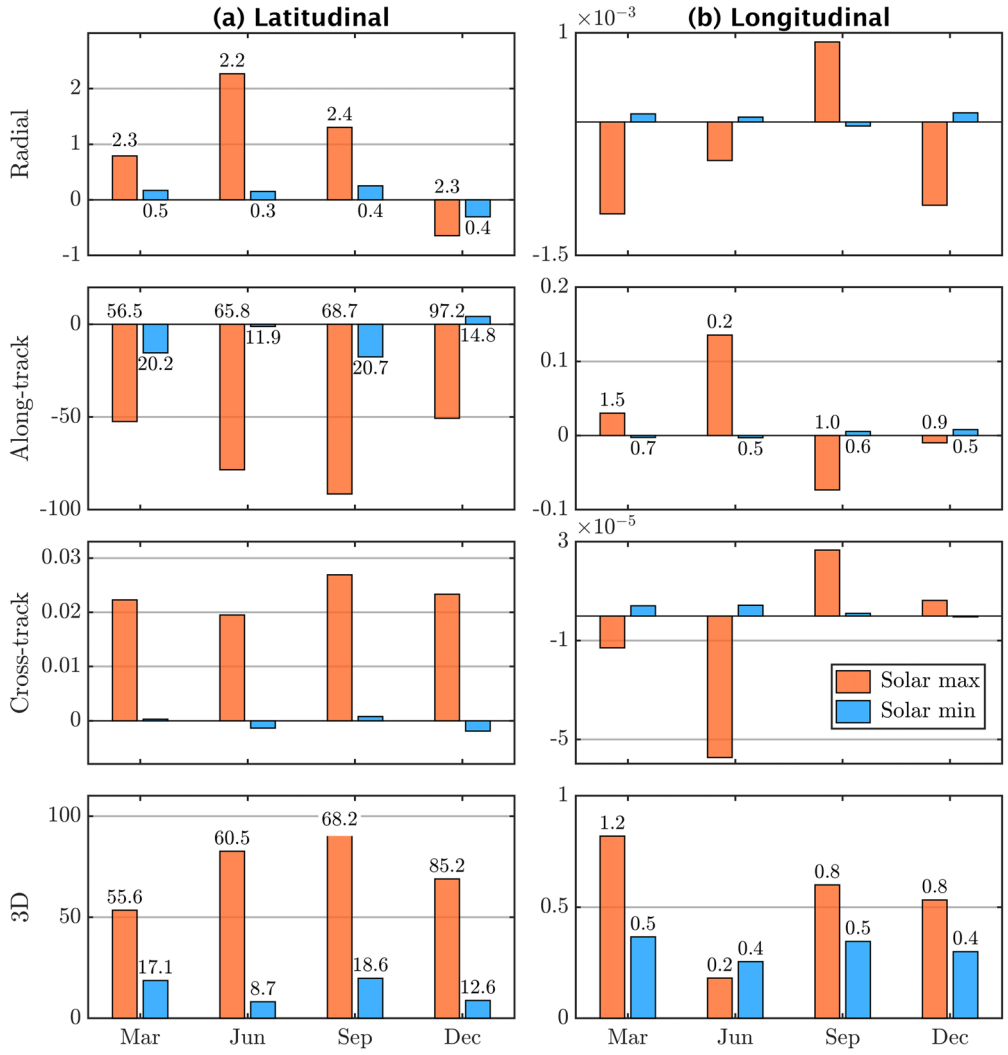

Figure 7. Impact of (a) latitudinal and (b) longitudinal variations in TMD on 1-day OP at 400 km during solar maximum and solar minimum (unit: m). The bars show the mean value of orbit difference between the control and reference orbits in radial, along-track and cross-track directions along with the three-dimensional (3-D) value. The values over/under the bar are the STD of orbit difference larger than 1 cm.

The influence of intradiurnal variations on 1-day OP is presented in Figure 6. Different from intra-annual variations, the mean value of the orbit difference in the along-track direction is close to zero and much smaller than the STD. These results indicate that intra-annual variations exert a systematic bias on 1-day OP but intradiurnal variations do not. It strongly suggests that a zero mean periodic variation in TMD only affects the predicted orbit if the prediction time is longer than the period of variation. Nevertheless, both intra-annual and intradiurnal variations enhance the uncertainty of the predicted orbit.

4.2. Large-Scale Spatial Impact

As shown in Figure 7, the orbit differences caused by the latitudinal and longitudinal TMD variations are much smaller than that of the temporal variations. During solar maximum, 3-D orbit difference for latitudinal variation is nearly 70 m. Note that the longitudinal variation due to the movement of subsolar point has been removed by using the same local solar time in DTM2013. The degree of the spherical harmonics used by DTM2013 is less than 6 (incomplete terms of the Legendre functions were adopted), and therefore, the impact of the horizontal variations shown here only include the horizontal variations with the wavelength larger than 30° (He et al., 2018).

Table 4
Mean and STD (in Parentheses) of Orbit Difference for the EMA (unit: m)

	Season	Radial	Along-track	3-D
Solar max	Mar	−0.16 (0.73)	16.5 (56.4)	47.1 (36.1)
	Jun	−0.05 (0.59)	6.7 (44.7)	39.1 (23.4)
	Sep	−0.19 (0.72)	14.3 (53.9)	45.2 (33.6)
	Dec	−0.21 (0.68)	16.6 (53.6)	44.6 (34.9)
Solar min	Mar	−0.03 (0.05)	3.0 (4.6)	4.3 (3.6)
	Jun	−0.02 (0.04)	1.8 (2.9)	2.6 (2.1)
	Sep	−0.03 (0.05)	2.3 (3.9)	3.5 (3.0)
	Dec	−0.03 (0.05)	2.3 (4.1)	3.5 (3.3)

Note. The result for the cross-track direction is not given due to its insignificant impact.

4.3. Impact of EMA and MDM

Table 4 presents the orbit difference in radial, along-track, and cross-track directions for a 1-day OP simulation for different seasons. The 3-D orbit difference can reach up to 50 m. The EMA tends to slightly accelerate the orbital decay because of the negative orbit difference in the radial direction.

In order to show more details on the influence of the EMA, the difference of the perigee distance, semimajor axis, eccentricity, and inclination for one example orbit is shown in Figure 8. The gray areas illustrate the time when the satellite passes the equatorial region during 10–20 LT. The differences in perigee distance and eccentricity clearly show the two peaks when the satellite enters and exits the EMA region.

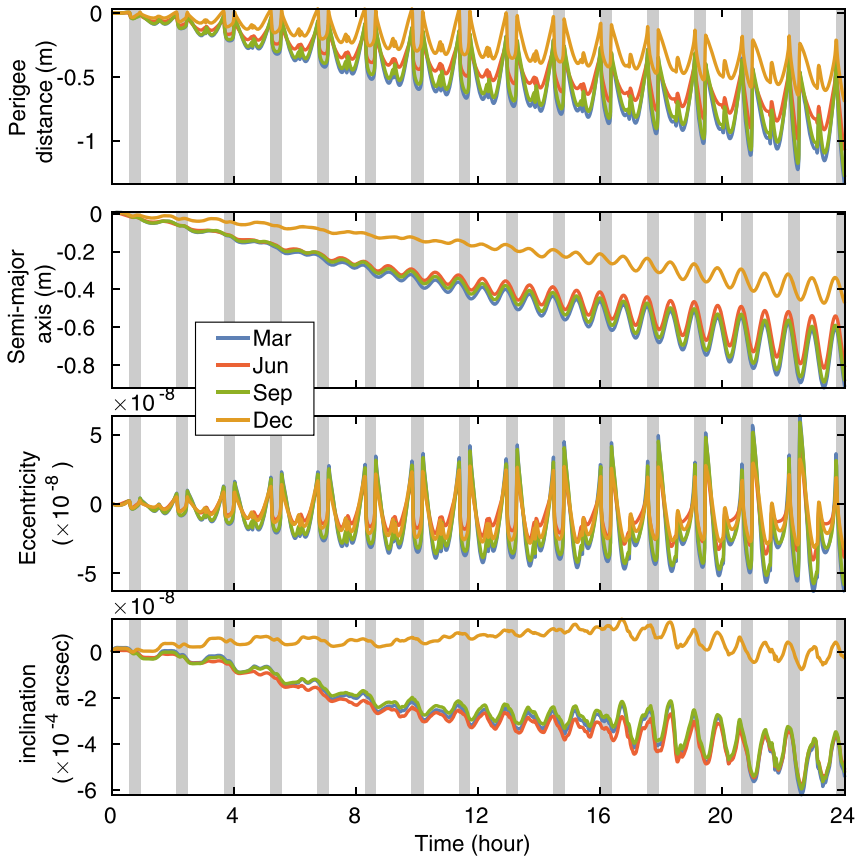

Figure 8. Orbit difference of a 1-day OP simulation for perigee distance, semimajor axis, eccentricity, and inclination (unit: m). The initial epochs of the OP simulation shown here are set to the same 00 LT. The gray areas illustrate the time when the satellite in the EMA region during 10–20 LT. Four colors indicate different seasons of the year.

Table 5
Mean and STD (in Parentheses) of Orbit Difference for the MDM (unit: m)

	Season	Radial	Along-track	3-D
Solar max	Mar	−2.35 (0.66)	180.4 (29.4)	182.8 (29.7)
	Jun	−1.36 (0.44)	100.8 (22.4)	102.2 (22.7)
	Sep	−2.54 (0.69)	186.0 (28.7)	188.6 (29.0)
	Dec	−1.55 (0.50)	121.0 (25.9)	122.6 (26.2)
Solar min	Mar	−0.09 (0.14)	7.5 (8.7)	10.5 (5.0)
	Jun	0.01 (0.15)	−1.4 (9.0)	6.9 (6.1)
	Sep	−0.10 (0.15)	8.0 (8.4)	10.6 (4.9)
	Dec	0.06 (0.15)	−3.6 (11.7)	8.5 (9.1)

Note. The result for the cross-track direction is not given due to its insignificant impact.

Although the percentage amplitude of MDM is higher than that of EMA, the mean orbit difference of MDM (<8 m) in the radial direction during solar minimum in Table 5 is much smaller than that of EMA (20–50 m) during solar maximum in Table 4. This can be explained by the fact that EMA is simulated in the daytime during solar maximum but MDM in the nighttime during solar minimum. The uncertainties in the along-track direction caused by both EMA and MDM are ~10 m.

5. Discussion and Conclusions

This study investigated the impact of different TMD variations on the orbital dynamics via a 1-day OP at a circular orbit of 400 km. The impact of TMD variations was analyzed using the differences between the orbits predicted with and without each specific TMD variation during solar minimum and solar maximum.

The empirical TMD model, DTM2013, was used to simulate the intra-annual, intradiurnal, and horizontal variations of TMD. It was found that DTM2013 showed an unexplainable midnight TMD maximum at 200 km in TMD (Figure S2). Although Bruinsma et al. (2017) reported the outperformance of DTM2013 at low altitude using the TMD data set derived from the Gravity Field and Steady-state Ocean Circulation Explorer satellite, their results are limited to the altitudes above ~240 km before 2014. Caution is hence required for the adoption of DTM2013 lower than 200 km. Due to this reason, OP simulation in the reentry regime (<200 km) has not been evaluated in this study.

The EMA and MDM features in the lower thermosphere were reproduced by simulating the field-aligned ion drag and atmospheric drag, respectively, in the physical TIE-GCM model. Their impact on orbital dynamics has been quantified separately in this study. However, many previous studies suggested a close relationship between them (e.g., Emmert, 2015b). Ma et al. (2010) found a nighttime EMA (peaked at 02 LT) in the CHAMP data. Miyoshi et al. (2011) estimated that ~50% of the magnitude in the EMA can be explained by the upward propagating terdiurnal tide from the troposphere, which is also closely connected to the MDM feature as previously discussed. To reveal the hidden connection between the EMA and MDM phenomena, future study will involve evaluating the tides during high solar activity and the field-aligned ion drag during low solar activity in TIE-GCM.

Table 6
Impact of TMD Variations on the 1-Day OP at 400 km

	Errors	
TMD variation	Solar max	Solar min
Annual	300 (20)	25 (5)
Semiannual	800 (40)	70 (15)
Diurnal	50 (30)	10 (10)
Semidiurnal	100 (100)	10 (10)
Terdiurnal	1 (1)	0.5 (0.5)
Latitudinal	50 (40)	15 (10)
Longitudinal	1 (1)	0.5 (0.5)
EMA	50 (30)	5 (3)
MDM	150 (30)	15 (6)

Note. The values inside and outside of the parentheses are the seasonal mean and STD (unit: m). EMA = equatorial mass anomaly; MDM = midnight density maximum.

Besides, the capability in capturing these types of variations can be a metric to evaluate the performance of TMD models. Meanwhile, it also helps to improve the understanding of the thermosphere and further optimizes the OP-oriented empirical TMD models.

The TMD variations are shown to have a notable impact on the orbit dynamics. Table 6 summarizes the uncertainty level of the TMD variations considered in this study. The value inside the parentheses is the STD of orbit difference. The impact of TMD on 1-day OP during solar maximum is far

larger than that during solar minimum. As expected, TMD variations have the largest impact in the direction of atmospheric drag, that is, the along-track direction.

The orbit difference caused by annual variation in the along-track direction is approximately 200–400 m (15–30 m) during solar maximum (minimum). The orbit difference due to the semiannual variation is nearly two times as large as that due to the annual variation. The orbit differences in radial, along-track, and cross-track directions also present clear seasonal fluctuations. Zero mean periodic variations have not significantly change the predicted orbit unless the period of the variation is much longer than the period of OP.

The orbit of 1-day OP at 400 km can be perturbed by the EMA with a magnitude of 50 m (5 m) during high (low) solar activity. The differences of both the perigee distance and eccentricity reveal a clear two-maxima feature before and after the satellite enters into the EMA region (geomagnetic latitude $< 30°$ and 10–20 LT). It was also found that the low Earth orbital dynamics is more sensitive to MDM (or atmospheric tides) than EMA (or field-aligned ion drag), which suggests that the upward propagating atmospheric tides resulting in the MDM have a stronger impact on LEO than that of the field-aligned ion drag resulting in the EMA.

This study demonstrates its necessity and potentials in balancing the efficiency and precision of OP for LEO missions. The selection of the TMD variations in OP can be determined by the accuracy needs of specific operational missions without boosting the computational burden. Further work is required to explore the impact of TMD variations which are not discussed in this study, for example, the short-term variation incurred by geomagnetic storms and substorms.

Acronyms

EMA Equatorial Mass Anomaly
LEO Low Earth Orbit
MDM Midnight Density Maximum
OP Orbit Prediction
TIE-GCM Thermosphere-Ionosphere-Electrodynamics General Circulation Model
TMD Thermospheric Mass Density

Acknowledgments
Sean Bruinsma at CNES is thanked for providing the source code of the DTM2013 model. Many thanks to the HAO team for giving access to the TIE-GCM (http://www.hao.ucar.edu/modeling/tgcm/tie.php). Jiuhou Lei and Haibing Ruan from the University of Science and Technology of China are thanked for their help and advice in reproducing the EMA and MDM using TIE-GCM. Changyong He thanks Stanley C. Solomon at HAO/NCAR for providing help in modifying the diffusion dynamics of TIE-GCM. The models of IERS 2010 Conventions used in the orbit prediction are publicly available online (http://iers-conventions.obspm.fr/conventions_material.php). This study was supported by the Cooperative Research Centre for Space Environment Management (SERC Limited) through the Australian Government's Cooperative Research Centre Programme and partially supported by the National Natural Science Foundation of China (41874040) and the CUMT Independent Innovation Project of "Double-First Class" Construction (2018ZZCX08). We would like to acknowledge the support of the Jiangsu dual creative talents and team projects. We would also like to thank the editor and two anonymous reviewers for their constructive comments.

References

Berger, C., Biancale, R., Ill, M., & Barlier, F. (1998). Improvement of the empirical thermospheric model DTM: DTM94—A comparative review of various temporal variations and prospects in space geodesy applications. *Journal of Geodesy*, *72*(3), 161–178. https://doi.org/10.1007/s001900050158

Bowman, B. R., Tobiska, W. K., Marcos, F. A., Huang, C. Y., Lin, C. S., & Burke, W. J. (2008). A new empirical thermospheric density model JB2008 using new solar and geomagnetic indices. In *Aiaa/aas astrodynamics specialist conference and exhibit*, pp. 6438. https://doi.org/10.2514/6.2008-6438

Bruinsma, S. (2015). The DTM-2013 thermosphere model. *Journal of Space Weather and Space Climate*, *5*, A1. https://doi.org/10.1051/swsc/2017008

Bruinsma, S., Arnold, D., Jaggi, A., & Sanchez-Ortiz, N. (2017). Semi-empirical thermosphere model evaluation at low altitude with GOCE densities. *Journal of Space Weather and Space Climate*, *7*, A4. https://doi.org/10.1051/swsc/2017003

Bruinsma, S., Thuillier, G., & Barlier, F. (2003). The DTM-2000 empirical thermosphere model with new data assimilation and constraints at lower boundary: Accuracy and properties. *Journal of Atmospheric and Solar-Terrestrial Physics*, *65*(9), 1053–1070. https://doi.org/10.1016/S1364-6826(03)00137-8

de Wit, T. D., & Bruinsma, S. (2017). The 30 cm radio flux as a solar proxy for thermosphere density modelling. *Journal of Space Weather and Space Climate*, *7*, A9. https://doi.org/10.1051/swsc/2017008

de Wit, T. D., Bruinsma, S., & Shibasaki, K. (2014). Synoptic radio observations as proxies for upper atmosphere modelling. *Journal of Space Weather and Space Climate*, *4*, A06. https://doi.org/10.1051/swsc/2014003

Doornbos, E. (2012). *Thermospheric density and wind determination from satellite dynamics*: Springer. https://doi.org/10.1007/978-3-642-25129-0

Doornbos, E., Klinkrad, H., & Visser, P. (2008). Use of two-line element data for thermosphere neutral density model calibration. *Advances in Space Research*, *41*(7), 1115–1122. https://doi.org/10.1016/j.asr.2006.12.025

Drob, D. P., Emmert, J. T., Meriwether, J. W., Makela, J. J., Doornbos, E., Conde, M., et al. (2015). An update to the horizontal wind model (HWM): The quiet time thermosphere. *Earth and Space Science*, *2*, 301–319. https://doi.org/10.1002/2014EA000089

Emmert, J. T. (2015a). Altitude and solar activity dependence of 1967–2005 thermospheric density trends derived from orbital drag. *Journal of Geophysical Research: Space Physics*, *120*, 2940–2950. https://doi.org/10.1002/2015JA021047

Emmert, J. T. (2015b). Thermospheric mass density: A review. *Advances in Space Research*, *56*, 773–824. https://doi.org/10.1016/j.asr.2015.05.038

Forbes, J. M., Bruinsma, S. L., Zhang, X., & Oberheide, J. (2009). Surface-exosphere coupling due to thermal tides. *Geophysical Research Letters*, *36*, L15812. https://doi.org/10.1029/2009GL038748

Foster, B. (2016). TIEGCM documentation, release 2.0 (Report). Boulder, USA: National Center for Atmospheric Research/High Altitude Observatory.

Giza, D., Singla, P., & Jah, M. (2009). An approach for nonlinear uncertainty propagation: Application to orbital mechanics. In *AIAA Guidance, Navigation, and Control Conference*, Chicago, pp. 1–19. https://doi.org/10.2514/6.2009-6082
Guo, J., Wan, W., Forbes, J. M., Sutton, E., Nerem, R. S., & Bruinsma, S. (2008). Interannual and latitudinal variability of the thermosphere density annual harmonics. *Journal of Geophysical Research*, *113*, A08301. https://doi.org/10.1029/2008JA013056
Hagan, M. E., & Forbes, J. M. (2002). Migrating and nonmigrating diurnal tides in the middle and upper atmosphere excited by tropospheric latent heat release. *Journal of Geophysical Research*, *107*(D24), 4754. https://doi.org/10.1029/2001JD001236
Hargreaves, J. K. (1992). *The solar-terrestrial environment: An introduction to geospace-the science of the terrestrial upper atmosphere, ionosphere, and magnetosphere*: Cambridge University Press. https://doi.org/10.1017/CBO9780511628924
He, C., Yang, Y., Carter, B., Kerr, E., Wu, S., Deleflie, F., et al. (2018). Review and comparison of empirical thermospheric mass density models. *Progress in Aerospace Sciences*, *103*, 31–51. https://doi.org/10.1016/j.paerosci.2018.10.003
Hsu, V. W., Thayer, J. P., Lei, J., & Wang, W. (2014). Formation of the equatorial thermosphere anomaly trough: Local time and solar cycle variations. *Journal of Geophysical Research: Space Physics*, *119*, 10,456–10,473. https://doi.org/10.1002/2014JA020416
Kasdin, N. J. (1995). Runge-Kutta algorithm for the numerical-integration of stochastic differential-equations. *Journal of Guidance Control and Dynamics*, *18*(1), 114–120. https://doi.org/10.2514/3.56665
Lechtenberg, T., McLaughlin, C. A., Locke, T., & Krishna, D. M. (2013). Thermospheric density variations: Observability using precision satellite orbits and effects on orbit propagation. *Space Weather*, *11*, 34–45. https://doi.org/10.1029/2012SW000848
Lei, J., Forbes, J. M., Liu, H.-L., Dou, X., Xue, X., Li, T., & Luan, X. (2011). Latitudinal variations of middle thermosphere: Observations and modeling. *Journal of Geophysical Research*, *116*, A12306. https://doi.org/10.1029/2011JA017067
Lei, J., Thayer, J. P., Wang, W., Luan, X., Dou, X., & Roble, R. (2012). Simulations of the equatorial thermosphere anomaly: Physical mechanisms for crest formation. *Journal of Geophysical Research*, *117*, A06318. https://doi.org/10.1029/2012JA017613
Lei, J., Thayer, J. P., Wang, W., Richmond, A. D., Roble, R., Luan, X., et al. (2012). Simulations of the equatorial thermosphere anomaly: Field-aligned ion drag effect. *Journal of Geophysical Research*, *117*, A01304. https://doi.org/10.1029/2011JA017114
Leonard, J. M., Forbes, J. M., & Born, G. H. (2012). Impact of tidal density variability on orbital and reentry predictions. *Space Weather*, *10*, S12003. https://doi.org/10.1029/2012SW000842
Liu, H., Thayer, J., Zhang, Y., & Lee, W. K. (2017). The non-storm time corrugated upper thermosphere: What is beyond MSIS? *Space Weather*, *15*, 746–760. https://doi.org/10.1002/2017SW001618
Ma, R. P., Xu, J. Y., Wang, W. B., Lei, J., Liu, H. L., Maute, A., & Hagan, M. E. (2010). Variations of the nighttime thermospheric mass density at low and middle latitudes. *Journal of Geophysical Research*, *115*, A12301. https://doi.org/10.1029/2010JA015784
Mayer-Guerr, T., Kurtenbach, E., & Eicker, A. (2010). ITG-Grace2010: The new GRACE gravity field release computed in Bonn. In *Egu General Assembly Conference Abstracts*, *12*, pp. 2446.
McLandress, C., Ward, W. E., Fomichev, V. I., Semeniuk, K., Beagley, S. R., McFarlane, N. A., & Shepherd, T. G. (2006). Large-scale dynamics of the mesosphere and lower thermosphere: An analysis using the extended Canadian Middle Atmosphere Model. *Journal of Geophysical Research*, *111*, D17111. https://doi.org/10.1029/2005JD006776
Miyoshi, Y., Fujiwara, H., Jin, H., Shinagawa, H., Liu, H., & Terada, K. (2011). Model study on the formation of the equatorial mass density anomaly in the thermosphere. *Journal of Geophysical Research*, *116*, A05322. https://doi.org/10.1029/2010JA016315
Petit, A., & Lemaitre, A. (2016). The impact of the atmospheric model and of the space weather data on the dynamics of clouds of space debris. *Advances in Space Research*, *57*, 2245–2258. https://doi.org/10.1016/j.asr.2016.03.005
Petit, G., & Luzum, B. (2010). IERS Conventions (2010) (IERS Technical Note 36). France: International Earth Rotation and Reference Systems Service.
Picone, J. M., Hedin, A. E., Drob, D. P., & Aikin, A. C. (2002). NRLMSISE-00 empirical model of the atmosphere: Statistical comparisons and scientific issues. *Journal of Geophysical Research*, *107*(A12), 1468. https://doi.org/10.1029/2002JA009430
Qian, L., & Solomon, S. C. (2012). Thermospheric density: An overview of temporal and spatial variations. *Space Science Reviews*, *168*(1-4), 147–173. https://doi.org/10.1007/s11214-011-9810-z
Richmond, A. D., Ridley, E. C., & Roble, R. G. (1992). A thermosphere/ionosphere general circulation model with coupled electrodynamics. *Geophysical Research Letters*, *19*(6), 601–604. https://doi.org/10.1029/92GL00401
Ruan, H. B., Du, J., Cook, M., Wang, W. B., Yue, J., Gan, Q., et al. (2015). A numerical study of the effects of migrating tides on thermosphere midnight density maximum. *Journal of Geophysical Research: Space Physics*, *120*, 6766–6778. https://doi.org/10.1002/2015JA021190
Ruan, H. B., Lei, J., Dou, X. K., Wan, W. X., & Liu, Y. C. M. (2014). Midnight density maximum in the thermosphere from the CHAMP observations. *Journal of Geophysical Research: Space Physics*, *119*, 3741–3746. https://doi.org/10.1002/2013ja019566
Shi, C., Li, W. W., Li, M., Zhao, Q. L., & Sang, J. Z. (2015). Calibrating the scale of the NRLMSISE00 model during solar maximum using the two line elements dataset. *Advances in Space Research*, *56*, 1–9. https://doi.org/10.1016/j.asr.2015.03.024
Sutton, E. K., Thayer, J. P., Wang, W., Solomon, S. C., Liu, X., & Foster, B. T. (2015). A self-consistent model of helium in the thermosphere. *Journal of Geophysical Research: Space Physics*, *120*, 6884–6900. https://doi.org/10.1002/2015JA021223
Vallado, D. A., & McClain, W. D. (2001). *Fundamentals of astrodynamics and applications* (Vol. 12): Springer Science and Business Media.
Xiong, C., Zhou, Y. L., Luhr, H., & Ma, S. Y. (2015). Tidal signatures of the thermospheric mass density and zonal wind at midlatitude: CHAMP and GRACE observations. *Annales Geophysicae*, *33*, 185–196. https://doi.org/10.5194/angeo-33-185-2015
Xu, J. Y., Wang, W. B., & Gao, H. (2013). The longitudinal variation of the daily mean thermospheric mass density. *Journal of Geophysical Research: Space Physics*, *118*, 515–523. https://doi.org/10.1029/2012JA017918
Zhu, X., Talaat, E. R., Baker, J. B. H., & Yee, J.-H. (2005). A self-consistent derivation of ion drag and joule heating for atmospheric dynamics in the thermosphere. *Annales Geophysicae*, *23*, 3313–3322. https://doi.org/10.5194/angeo-23-3313-2005

Erratum

The originally published version of Table 3 contained an error. The exponents in the description of the last row should be negative but were typeset as positive. The version that underwent peer review used negative exponents. This error has been corrected, and the current version may be considered the version of record.